

Radio Emission from Young Supernovae and Supernova Remnants in Arp 299

James S. Ulvestad

National Radio Astronomy Observatory

P.O. Box 0, Socorro, NM 87801

julvesta@nrao.edu

ABSTRACT

We have made sensitive milliarcsecond-resolution radio images of the nearby merger galaxy Arp 299 at four epochs spread over 18 months between 2003 and 2005. The combined data revealed a total of 30 point sources in the two primary merger nuclei. Twenty-five of these are found in the northeastern nucleus (component “A”=IC 694) over a region ~ 100 pc in diameter, while 5 are in the southwestern nucleus (component “B1”=NGC 3690) within a region ~ 30 pc in size. These objects are interpreted as young supernovae and supernova remnants; the ratio of the source counts in nuclei A and B1 is approximately equal to the ratio of their predicted supernova rates. An approximate luminosity function has been derived for nucleus A, and indicates that it might contain as many as 500–1000 compact radio sources more powerful than Cas A; the integrated flux density of these sources would be about 20% of the total flux density seen at lower resolution. A new supernova occurred in nucleus B1 in the first half of 2005, having a peak radio power at least 2,000 times the present power of Cassiopeia A. This supernova is located within 0.4 pc (projected distance) of an apparently older supernova remnant, making it very likely that this indicates the presence of a massive super star cluster within nucleus B1. Comparison of the typical radio flux densities of our compact radio sources to the observed X-ray luminosities of nuclei A and B1 indicates that it is possible that one radio source in each nucleus actually could be associated with an active galactic nucleus rather than being a supernova remnant.

Subject headings: galaxies: starburst — galaxies: evolution — galaxies: individual (Arp 299, NGC 3690, IC 694) — supernovae: general — radio continuum: galaxies

1. Introduction

It now appears likely that the most massive galaxies in the universe formed from multiple mergers of smaller galaxies; those mergers are apparent in the disturbed morphologies of many galaxies imaged in deep optical and infrared fields such as the Hubble Deep Fields (Ferguson et al. 2000), the GOODS survey (Dickinson et al. 2003; Giavalisco et al. 2004), and the COSMOS survey (Scoville et al. 2007). Nearby and present-day analogs of these early galaxies often are found in Luminous and Ultraluminous Infrared Galaxies, many of which are undergoing major mergers at the present epoch. The nearest major merger galaxy is generally regarded as the ‘Antennae,’ NGC 4038/9 (Whitmore et al. 1999), at a distance of 20 Mpc. Other nearby infrared-bright galaxies undergoing major mergers are Arp 299 (Gehrz et al. 1983; Meurer et al. 1995; Alonso-Herrero et al. 2000), NGC 3256 (Norris & Forbes 1995; Kotilainen et al. 1996; Lípári et al. 2000), and Arp 220 (Soifer et al. 1999; Rovilos et al. 2003; Lonsdale et al. 2006; Parra et al. 2007). The starbursts in these mergers and other galaxies obey the so-called “radio-infrared relation”, whereby their radio and far-infrared powers are well-correlated (Condon 1992); the infrared emission is thought to be powered ultimately by the photons from hot young stars, while the radio emission typically is powered by synchrotron radiation from particles accelerated in supernovae (SNe) and supernova remnants (SNRs).

In recent years, compact radio sources have been used as one window providing insights into the nature of merger/starburst galaxies. In the most nearby starbursts, such as M82 (Muxlow et al. 1994; Fenech et al. 2008) and NGC 253 (Ulvestad & Antonucci 1997; Lenc & Tingay 2006), interferometers reveal a mix of thermal and nonthermal radio sources representing H II regions and fairly young SNRs. However, in the somewhat more distant merger galaxies, typically at distances of a few tens of megaparsecs, use of the Very Long Baseline Interferometry (VLBI) technique is required to separate individual compact sources; the interferometer sensitivity on continent-scale baselines is insufficient to detect H II regions, so only non-thermal emission from young SNe and SNRs is detected. For example, a series of observations of the merger galaxy Arp 220 (Rovilos et al. 2003; Lonsdale et al. 2006; Parra et al. 2007) has detected at least 49 objects in the two merger nuclei, provided the radio spectra of many of these objects, and detected the explosion of several new supernovae.

The subject of our investigation is the relatively nearby (41 Mpc) merger galaxy Arp 299 (Mrk 171), which was noted as a starburst galaxy over 25 years ago by Gehrz et al. (1983). The two primary nuclei of the merger are the northeastern component A (often referred to as IC 694) and the southwestern component B (often referred to as NGC 3690). Although we focus primarily on the starburst in this paper, one or both nuclei also have been inferred to contain active galaxy components based on X-ray imaging and spectroscopy (Della Ceca et al.

2002; Zezas et al. 2003; Ballo et al. 2004), optical integral-field spectroscopy (García-Marín et al. 2006), and the presence of nuclear H₂O masers (Henkel et al. 2005; Tarchi et al. 2007).

There is substantial CO emission associated with the Arp 299 starburst, and a relatively high ratio of HCN/CO at the two primary nuclei, implying the presence of dense and warm molecular clouds in the two nuclei (Aalto et al. 1997). Baan & Haschick (1990) found OH megamaser emission from nucleus A, and inferred that this emission comes from a clumpy molecular medium located 100–600 pc in front of the continuum radio source(s) being amplified. Near-infrared imaging and modeling of Arp 299 by Alonso-Herrero et al. (2000) have shown that nucleus A accounts for 50% of the near-infrared emission of the merger and has a star-formation and supernova rate approximately six times those of nucleus B. The latter nucleus actually is resolved into a dominant component B1, and a weaker component B2 located an arcsecond to the NW (Lai et al. 1999; Alonso-Herrero et al. 2000; Neff et al. 2004). In order to provide context to the reader, we reproduce two previously published figures here. Figure 1 is an 814 nm *Hubble Space Telescope* image of Arp 299, while Figure 2 is a high-resolution Very Large Array (VLA) image of the merger at radio wavelengths, both reproduced from Neff et al. (2004).

Arp 299 has hosted at least five optical supernovae in the last 20 years, the last of which was the type II supernova SN 2005U (Mattila et al. 2005; Modjaz et al. 2005). These optical supernovae all occurred outside the primary merger nuclei; those nuclei are likely to be the most frequent sources of supernovae in Arp 299, but their extreme obscuration makes finding optical supernovae highly unlikely. Even a two-epoch NICMOS near-infrared search failed to reveal any new supernovae in the two merger nuclei (Cresci et al. 2007). However, high-resolution VLBI imaging of Arp 299 revealed five compact radio sources in nucleus A, including at least one very young supernova (Neff et al. 2004).

This paper reports VLBI observations of Arp 299 with considerably higher sensitivity than those of Neff et al. (2004), aimed at probing deeper into the radio luminosity function and searching for the onset of radio emission from young supernovae.

2. VLBI Observations

The merger system Arp 299 was observed on four occasions using an interferometer including the Very Long Baseline Array (VLBA) augmented by the Robert C. Byrd Green Bank Telescope (GBT). The VLBA (Napier et al. 1993) is an interferometer consisting of 10 identical 25m antennas distributed from Hawaii to the US Virgin Islands, while the GBT is a 100m x 110m single aperture in West Virginia, which was added to the VLBA in order

to approximately double the overall sensitivity of the array. Observations were carried out under program code BU027, and took place at approximately six-month intervals between late 2003 and mid-2005.

Each of the four observing epochs consisted of almost identical 10-hr sessions. At each epoch, blocks of 60–110 minutes were alternated between sky frequencies of 2.2715 GHz (hereafter 2.3 GHz) and 8.4215 GHz (hereafter 8.4 GHz). There were four blocks at 2.3 GHz and three blocks at 8.4 GHz; 2.3-GHz observing blocks were placed at the beginning and end of each 10-hr session in order to minimize the impact of atmospheric water vapor fluctuations in low-elevation observing at 8.4 GHz. At each band, four 8-MHz frequency channels were used at both right and left circular polarizations. All were sampled at the Nyquist rate with two bits per sample, providing a total data rate of 256 Mbit s⁻¹. These data were recorded on a mix of instrumentation tapes and hard-disk modules which were shipped to Socorro, New Mexico for processing on the VLBA correlator. Only the parallel polarization hands were processed, in order to keep the data rate within the correlator output limits; each 8-MHz frequency band was further subdivided into 32 or 64 spectral channels in order to preserve the capability for wide-field imaging.

The GBT was typically missing for 10%–20% of the time in each observing session, due to software and pointing problems as well as 5–10 minute periods to change between 2.3 and 8.4 GHz. The Mauna Kea VLBA antenna did not observe in the first and third epochs due to bad weather. The Kitt Peak VLBA antenna had 25% of its 2.3 GHz data removed in all observations, due to bad interference in one of the 8-MHz bandpasses. Additional data losses were typically no more than 5%–10% of the data from 1–2 antennas for a given observing run and frequency band.

The observations were carried out in phase-referencing mode (Beasley & Conway 1995). Observations of 2.5 minutes in length on Arp 299 were interleaved with observations of approximately 45 seconds on the calibration source J1128+5925, located 0.86° from Arp 299. Both the antennas and the correlator were targeted midway between the strongest centimeter radio component, nucleus A of Arp 299, and the possible background source D, which were previously detected in the VLBI observations of Neff et al. (2004); this pointing preserved signal/noise in the relatively small beam of the GBT as well as minimizing the effects of bandwidth smearing. Occasional 2.5-minute observations of J1127+5650, located 2.58° from J1128+5925, were made in order to provide a check of the phase-referencing quality. Table 1 is a summary of the observations, including the observation dates and the total integration time on Arp 299 at each frequency band.

All data calibration was carried out in NRAO’s Astronomical Image Processing System, AIPS (Greisen 2003). Standard corrections included those for Faraday effects in the Earth’s

ionosphere, application of the most accurate Earth orientation parameters, gain corrections to remove the effects of non-optimal sampler levels, and calibration of the feed rotation of the individual antennas. Initial coarse solutions for the interferometer delays were provided by fitting one or two scans of a strong calibrator (usually J0927+3902=4C 39.25), while final delay and phase calibration (or “fringe fitting”) was performed by least-squares fitting on each 45-second scan of J1128+5925. The resulting delay and phase solutions were interpolated in time to provide the final calibration of Arp 299 and the check source.

Particular care was taken in setting the amplitude calibration scale for the GBT. VLBA antennas provided useful system temperature data at roughly 1-minute intervals, and their calibration is judged to be accurate at the 5% level. However, the *a priori* and real-time calibrations of the GBT were less accurate; good values for GBT are important because it is the most sensitive telescope in the observing array. Nominal values for GBT sensitivity were used to weight the GBT during the fringe-fitting process. Then the amplitude scale was adjusted so that the flux densities of the amplitude-check sources J0854+2006 (OJ 287) and J1310+3220 varied smoothly with baseline length; in this adjustment, care was taken to make the amplitude on interferometer baselines to the GBT similar to those involving the relatively nearby VLBA antenna in Hancock, New Hampshire. This is a subjective process because source structure is convolved with the fringe pattern for each individual baseline, so the final calibration was determined “by eye” using the source flux-density plots. Adjustments of the GBT sensitivity relative to the nominal values were as high as 25%, but more typically in the 10% range.

3. Imaging, Source Identification, and Flux-Density Measurements

3.1. Imaging

For each data set, images were produced using the standard deconvolution and “Clean” algorithms in AIPS. Initially, six fields were imaged in each data set, centered on the six strongest and most compact VLA sources detected by Neff et al. (2004). These six regions were the two primary nuclei of the galaxy merger, A and B1; source B2 to the NW of B1; the two possible additional merger nuclei, C and C’; and the possible background source D. Each field consisted of a 1’024-square image centered on the position of the appropriate compact VLA source, with at least four pixels per resolution element. The data sets were Cleaned to minimum flux-density levels of 3–4 times the predicted noise for each image, in order to assure that sidelobes due to imperfect sampling were removed completely.

Careful source identification procedures, discussed in Section 3.2, were carried out on all

six fields. The only significant detections in individual epochs or in combined data from all four epochs were found in the fields A, B1, and D. Therefore, to avoid generating spurious sources by cleaning noise spikes, we produced the final interferometer images by targeting only the three fields with detected sources; this improved the noise characteristics of the final images by $\sim 10\%$. The noise levels from the final three-field images are cited in Table 1, and are typically 10%–20% above the theoretical values under ideal conditions. The effective noise levels were somewhat higher because of imperfect phase referencing, as discussed in Section 3.3.

After making the initial images, we experimented with self-calibration in order to refine the atmospheric calibration and hence improve the final images of Arp 299. However, because there is very little correlated signal present, adequate signal/noise required averaging times considerably longer than the atmospheric coherence time, so self-calibration was not effective. Thus, we depended instead on the data with only the phase calibration relative to J1128+5925.

The purposes of the four epochs of observation were twofold—both to achieve a time baseline long enough to see source flux density changes, including the appearance of new sources, and to achieve sufficient integration time to go significantly deeper than the VLBA+GBT observations by Neff et al. (2004). For the latter purpose, it is necessary to combine all the data from four epochs. The traditional ways to do this are to (1) combine the calibrated data from all four epochs in order to make a single set of images, or (2) average the four-epoch images in the image plane. The former method may be susceptible to errors in the case of significant source variability, while the latter method does not easily retain the relative weighting of the different baselines or of observations with different noise and dynamic range levels. We chose the first method, combining the calibrated data sets and then producing three-field images of the combined data as for the individual epochs. Figures 3 and 4 show the final 2.3 GHz images of the regions of nuclei A and B1 containing all the detected compact radio sources. Images of the same fields at 8.4 GHz are not shown because of the smaller number of sources detected in that band. From these figures, we note that the compact radio sources in nucleus A extend over a region ~ 100 pc in diameter, while the compact sources in nucleus B1 are all found within a region ~ 30 pc in diameter.

3.2. Source Identification

The final source identification within the fields of A, B1, and D proceeded in an iterative process. First, all individual peaks above five times the rms noise were identified in the 2.3-GHz images, and peaks above six times the rms noise were identified at 8.4 GHz, both

at the individual epochs and in the combined data sets. (The higher noise threshold at 8.4 GHz is caused by the fact that the 8.4 GHz images have 16 times as many pixels as the 2.3 GHz images.) At some individual epochs, there were apparently spurious sources above the cutoff flux densities near the strongest (~ 1 mJy) sources, almost certainly due to the imperfect phase-referencing. These spurious sources were easily identified because they occurred at different locations at the different epochs, and largely disappeared when data sets were combined.

Locations of all sources above the cutoffs in the images from the combined data sets were inspected at each individual epoch. Sources exceeding the nominal cutoff in the combined images were considered real if individual peaks above 2.5σ also could be identified in at least two of the four epochs; alternatively, if a peak above 7σ that was not an obvious image defect could be found in a single epoch, a source was considered real and possibly variable. In fact, using these criteria for the individual epochs, all sources above the cutoffs in the combined data sets were found to be real, and we judge the source identification to be complete at the 5σ (2.3 GHz) and 6σ (8.4 GHz) levels for the combined data sets.

3.3. Source Flux Densities and Positions

For weak source detections, some sources can appear slightly resolved because of noise plateaus lying near the actual sources. In our images, no sources were obviously resolved when this effect was taken into account; given unresolved sources, the flux densities may be measured by a variety of methods. We chose to make quadratic fits to the inner few pixels of each source in order to determine the peak flux density, and used this value as the total flux density for the apparently unresolved sources. An alternative method of fitting beam-sized gaussians to each source makes assumptions about flux-density distributions that may not be warranted, particularly in the situation where imperfect phase-referencing scatters flux non-randomly in the image plane.

As stated previously, the phase-referencing process corrects imperfectly for the troposphere and ionosphere. Thus, there is a net coherence loss in the Arp 299 images, and an apparent reduction in correlated flux densities. We measured this reduction by using the phase-reference check source, J1127+5650 (hereafter J1127). J1127 was imaged using the initial phase calibration applied from J1128+5925, then self-calibrated and re-imaged. The increase in peak flux density by this procedure was a measure of the loss of coherence due to the phase referencing errors. The reduction in flux density for Arp 299 at each epoch then was estimated by multiplying the coherence loss of J1127 by the ratio of separations from the calibrator, ($0.86^\circ/2.58^\circ$), since the coherence loss should depend approximately linearly on

the separation between reference and target source (Beasley & Conway 1995). Table 2 gives the flux-density correction factor for Arp 299 inferred by this method for each epoch, the average correction factor over the four epochs, and the “real” noise levels achieved for the combined data sets after the imperfect phase-referencing is taken into account. Inspection of Table 2 indicates that the 2.3 GHz coherence losses were more consistent from epoch to epoch, while the 8.4 GHz coherence losses were much worse during the northern summer; this supports the inference that the 2.3-GHz losses were dominated by an ionospheric calibration error whose magnitude is relatively independent of season, while the 8.4-GHz losses were dominated by the troposphere, which is more variable during the summer. Final flux densities for the Arp 299 sources were obtained by multiplying the fitted flux densities by the amplitude correction factor at each epoch, or by the average correction factor for the combined data sets.

Errors in flux-density estimates have three different causes. First, there is an overall scale error, dominated by the error in calibrating the GBT, which we estimate to be 10% (see Section 2). Second, there is an error in estimating the coherence loss, including the assumptions that this loss depends linearly on target/calibrator separation, is otherwise independent of direction, and has the same temporal structure for Arp 299 and J1127 (the latter source was observed only every hour or two). We take this error to be 50% of the inferred coherence loss; i.e., for an apparent coherence loss of 15%, the 1σ error in the loss factor is assumed to be 7.5%. (In reality, the error in coherence loss is surely non-gaussian, but there is no definitive reason to adopt any other form.) Third, there is the error caused by the limited signal/noise ratio of the data, which is as high as 20% for a 5σ source and as low as 3% for a 1-mJy source at a single epoch. We add these three errors in quadrature to derive the final errors at each epoch. For the final images using the combined data sets, we assumed that the flux-density scale errors and coherence-loss errors were uncorrelated from epoch to epoch, implying that they are reduced by a factor of two for four epochs.

Source position measurements are unaffected by amplitude scale errors. At 2.3 GHz, epoch-to-epoch position shifts should be dominated by signal/noise considerations, which limit the positional accuracy to approximately the beam size divided by the signal/noise ratio; this may be as large as 1 mas for a 5σ – 6σ source. At 8.4 GHz, position shifts between epochs sometimes are larger than the 0.2–0.3 mas that this simple assumption would indicate, most likely due to the imperfect phase calibration. We must also account for the uncertainty in the position of J1128+5925; errors are given by Fey et al. (2004) as 0.16 mas in right ascension and 0.27 mas in declination. In fact, the current VLBA calibrator list¹ was used;

¹(<http://www.vlba.nrao.edu/astro/calib/vlbaCalib.txt>)

it quotes 50% larger errors, and uses updated coordinates that differ from Fey et al. (2004) by about 0.05 mas in each coordinate. Given that the signal/noise at 2.3 GHz limits position determination to 1 mas accuracy for the weakest sources, and that the phase-referencing may limit 8.4 GHz positions at a similar level, we estimate position errors of 1.0 mas in each coordinate, and quote absolute source positions to an accuracy of 0.1 milliseconds of time in right ascension and 1.0 mas in declination.

Table 3 gives the final positions and flux densities of all our confirmed sources at 2.3 GHz, while Table 4 gives a similar list for 8.4 GHz. In these tables, source names are given by convention as position offsets from $\alpha_{J2000} = 11^h28^m$ and $\delta_{J2000} = 58^\circ33'$; for sources in common between both frequency bands, the source name derived from the 8.4 GHz position is used. The source properties and their implications are discussed further in section 4.

4. Discussion of Compact Radio Sources

4.1. Source Detection Summary

Inspection of Tables 3 and 4 shows that there are significant milliarcsecond radio sources detected in both of the primary nuclei of the galaxy mergers, A and B1; as stated in Section 3.1, there were no detections in B2, C, or C'. Source D is detected at all epochs, but with no other radio detections nearby. Neff et al. (2004) previously reported five VLBI detections in A, as well as detection of D, but none in B1. The much deeper observations described in this paper revealed 19 sources at 2.3 GHz in A, as well as 13 sources at 8.4 GHz; since only 7 objects were detected at both frequency bands, there are now a total of 25 distinct VLBI radio sources in A. In addition, there were four “steady” detections in B1, plus a variable source that only appeared at the fourth epoch. Since no sources are resolved at either 2.3 or 8.4 GHz, we infer that they generally have sizes smaller than one milliarcsecond, or 0.2 pc. The most likely interpretation, by virtue of analogy with similar sources in other merger or starburst galaxies such as Arp 220, M82, and NGC 253, is that the sources are all young, compact SNe or SNRs. In fact, the ratio of 5:1 in source counts between A and B1 is very close to the ratio of 5.9:1 in their estimated supernova rates (Alonso-Herrero et al. 2000), indicating that the stellar mass functions and supernova evolution may be similar between the two nuclei. In an extreme merger such as Arp 299, where much of the starburst has occurred in the last 10 Myr (Alonso-Herrero et al. 2000), it is likely that virtually all of the radio sources have resulted from Type II supernovae.

4.2. Source Variability

In Figure 5, we plot the four-epoch 2.3 GHz data and 8.4 GHz data for the strongest source at each band, one of intermediate strength, and one of the weaker sources. This figure includes data for only a few sources, but most of the detected sources show no significant variability. Since the error bars at individual epochs are typically in the 10%–15% range, the upper limits on variability over 18 months are only in the vicinity of 20% for the non-variable objects. These limits are consistent with the much smaller variability and limits seen in most radio sources in NGC 253, M82, and Arp 220 (Ulvestad & Antonucci 1994, 1997; Kronberg et al. 2000; Parra et al. 2007; Fenech et al. 2008).

We find only two sources in our program that display significant variability, both at 8.4 GHz. The first is the strongest 8.4 GHz source shown in the right-hand panel of Figure 5, designated as 33.621+46.71 in Table 4; this source in nucleus A appears to have a systematic flux density decline over four epochs. It was initially reported by Neff et al. (2004) as a very young radio supernova, and found to have an 8.4 GHz flux density of 3.2 mJy at epoch 2003.11; this higher flux density in early 2003 confirms the monotonic decline seen in Figure 5.

The other variable source at 8.4 GHz appeared only at the fourth epoch, in nucleus B1, as noted in Table 4 (source 30.988+40.78). Further discussion of this source is deferred until Section 4.5.

4.3. Source Spectra

Figure 6 shows the distribution of two-point spectral indices (α , defined by $S_\nu \propto \nu^{+\alpha}$) for all the detected sources except the new source that appeared at the fourth epoch; those sources with upper limits to their flux densities at 2.3 or 8.4 GHz are shown hatched. Errors in the values of α range from 0.09 to 0.19 for the sources detected at both frequencies, while the errors on the spectral-index limits for sources detected at only one frequency range from 0.16 to 0.21. Because only 8 of the 29 sources in this plot were detected at both frequencies, we have not attempted to find the true distribution of source spectra. Mathematically, one could use survival analysis to derive a hypothetical “true” spectral index distribution. However, this would rely on an implicit assumption that sources with upper limits at each frequency are distributed similarly to the sources detected at both frequencies, and this is very unlikely to be a correct assumption.

We can say that at least seven of the sources have positive spectral indices, almost surely indicating optically thick synchrotron emission. (Brightness temperatures of these

milliarcsecond sources are above 10^6 K for even the weakest sources, and thus the radio emission is highly unlikely to be thermal in nature.) The two variable sources, only one of which is included in Figure 6, have spectral indices $\alpha > +1.5$ between 2.3 and 8.4 GHz. Such steep positive spectra are characteristic of very young radio SNe which have become optically thin at the higher frequency, but remain optically thick at the lower frequency (Weiler et al. 2002). Hence we infer that the radio sources occupying the right side of Figure 6 are likely to be the most recent supernovae.

4.4. Radio Luminosity Functions

The distributions of radio luminosities at 2.3 and 8.4 GHz are shown in Figure 7, with the objects from nuclei A and B1 distinguished from one another. The detection thresholds are 1.7×10^{19} W Hz $^{-1}$ at 2.3 GHz and 1.8×10^{19} W Hz $^{-1}$ at 8.4 GHz. For reference, we compare these values to the galactic SNR Cassiopeia A. Using the spectrum and flux-density evolution of Cas A found by Baars et al. (1977), as well as the 3.4 kpc distance derived by Reed et al. (1995), we derive Cas A powers at epoch 2005.0 of 1.6×10^{18} W Hz $^{-1}$ at 2.3 GHz and 6.1×10^{17} W Hz $^{-1}$ at 8.4 GHz. Thus, our respective detection thresholds for milliarcsecond radio sources in Arp 299 are ~ 11 and ~ 29 times the Cas A power at 2.3 and 8.4 GHz.

It is of interest to compute the total number of radio sources that might be expected above the Cas A power in Arp 299, as this may provide some insights into the time evolution of the sources. We consider only nucleus A, since the number of radio sources in nucleus B1 is too small to derive useful statistical results. One can use the distribution of observed radio powers shown in Figure 7 to fit a luminosity function, and then integrate that luminosity function down to the power of Cas A. However, the small-number statistics give rather large errors on any such fit. For a rough estimate, we assume a power-law form for the luminosity function, and take bin widths of 0.2 dex in radio power. At $\log(P) = 19.75$ (in W Hz $^{-1}$), we ameliorate small-number statistics slightly by averaging this bin with the two adjacent bins, and find 2 sources per bin at 8.4 GHz and 2.33 sources per bin at 2.3 GHz. A two-point fit between these average values at $\log(P) = 19.75$ and the values at $\log(P) = 19.35$ gives the following results, where $P_{19} = P/(10^{19} \text{ W Hz}^{-1})$:

$$dN(P_{19})/d \ln P_{19} \sim 80P_{19}^{-2.6} \quad (1)$$

at 2.3 GHz, and

$$dN(P_{19})/d \ln P_{19} \sim 30P_{19}^{-2.2} \quad (2)$$

at 8.4 GHz. Integrating these estimated luminosity functions down to the luminosity of Cas A at the respective frequencies, we find that nucleus A of Arp 299 would contain approximately

890 sources stronger than Cas A at 2.3 GHz and 740 sources stronger than Cas A at 8.4 GHz. The error bars on these numbers are roughly a factor of two, based on relatively small-number statistics, and also ignore the possibility that the shapes of the luminosity functions might change at lower luminosities. Indeed, it is possible that most of the objects detected in our observations are fairly young radio SNe, whose emission still is largely dominated by interaction with their own mass-loss shells, rather than SNRs dominated by interaction with an external medium (Chevalier & Fransson 2001; Chevalier et al. 2004); any transition from SNe to SNRs most likely would cause the luminosity function to change shape. Extensive discussion of the SNe/SNR evolution in the merger Arp 220 is given by Parra et al. (2007), and we refer the interested reader to that paper for details that also may apply to Arp 299.

The summed flux densities of the observed young supernovae and supernova remnants in nucleus A (Tables 3 and 4) amount to 5.3 mJy at 2.3 GHz and 4.2 mJy at 8.4 GHz. Multiplying the above luminosity functions by power and integrating down to the power of Cas A, we find respective total flux densities of 19 and 14 mJy at 2.3 and 8.4 GHz, in compact radio sources more powerful than Cas A. Neff et al. (2004) gave respective flux densities of 101 and 77 mJy at 4.9 and 8.4 GHz in the sub-arcsecond component of nucleus A. Thus, even if the estimated luminosity functions continue unbroken to the power of Cas A, the total flux density in young SNe and SNRs more powerful than Cas A is only $\sim 15\text{--}20\%$ of the total radio flux density in nucleus A, consistent with all observations.

We can consider the implications of this result by comparing it with the expected supernova evolution in our own Galaxy. It has been ~ 330 yr since the supernova event that created Cas A (Hughes 1980), so one can examine the (admittedly naive) hypothesis that all supernovae in Arp 299 evolve exactly like Cas A. For a supernova rate of 0.65 yr^{-1} in nucleus A of Arp 299 (Alonso-Herrero et al. 2000), there should now be ~ 200 SNRs younger than Cas A in that nucleus, while integration of the estimated luminosity functions implies that Arp299-A may contain as many as ~ 800 SNRs above the Cas A power. This is weak evidence that the SNRs in Arp 299 stay stronger for a longer period of time, as one might expect if they explode in a dense medium and expand more slowly than in our own Galaxy. By comparison, the nearby starburst galaxies M82 and NGC 253 have $\sim 10\text{--}20$ radio SNRs more powerful than Cas A (Ulvestad & Antonucci 1997; Fenech et al. 2008) in galaxies with supernova rates of $\sim 0.1 \text{ yr}^{-1}$, which would scale to $\sim 60\text{--}120$ objects for supernova rates of $\sim 0.6 \text{ yr}^{-1}$. This implies that the SNR evolution may be more rapid, or the SNRs intrinsically less luminous, in these weaker starbursts. Alternatively, as suggested for Arp 220 by Parra et al. (2007), it may be that the initial mass function in the more extreme starburst galaxies is more top-heavy. However, the evidence for the existence of such top-heavy mass functions is inconclusive (Elmegreen 2005).

Given the large uncertainties in the luminosity function, a significantly deeper VLBI observation of Arp 299, which should be possible within 2–3 yr, would be required to test whether the young SNe and SNRs in Arp 299 are more radio-powerful or longer-lasting than those in less active starbursts. A turnover in the luminosity function that would be caused by a top-heavy initial mass function, as well as additional young supernovae, might be revealed by such an observation.

4.5. The Two Newest Supernovae

As mentioned in Section 4.2, we have detected two compact variable sources at 8.4 GHz, which we identify as young supernovae. First, we consider the source 33.621+46.71, previously denoted as A0 by Neff et al. (2004). This object had an 8.4 GHz flux density of 3.2 mJy at epoch 2003.11, and fell to 1.1 mJy at epoch 2005.55. Fitting an exponential falloff of the form $S(t) = S_0(t_0) (t/t_0)^{-b}$ since epoch 2003.11, we find that the source flux density at 8.4 GHz was declining as $t^{-0.63}$. However, since the source was not detected at 2.3 GHz at any of our four epochs, we conclude that it still remained optically thick at that frequency 2.5 yr after becoming optically thin at 8.4 GHz. The slow rise time at 2.3 GHz is consistent with a Type II supernova, but not a Type Ib/c supernova (see Table 3 of Weiler et al. 2002).

The other variable source was detected only at our last epoch, 2005.55, in Nucleus B1; it had an 8.4-GHz flux density of 1.17 ± 0.28 mJy at that time. We have no later VLBI observations to study its evolution, but we did search for all relevant observations in the VLA data archive. We found two **A** configuration observations that were taken subsequent to the many epochs of data analyzed by Neff et al. (2004). These observations were made under program code AC749, on 2004NOV02 (2004.84) and 2006APR15 (2006.29), and have resolution of $0''.2$. We have extracted both data sets from the VLA archive and analyzed them. Historically, the 8.4 GHz flux densities of nucleus B1 ranged from 5.9 to 7.2 mJy in **A** configuration data obtained between 1990 and 2002, while nucleus A ranged from 70 to 75 mJy (Neff et al. 2004). Thus, a new radio source with a flux density of a few millijansky or less would not be noticeable within nucleus A, but might be detectable in nucleus B1. Table 5 gives the results of our flux-density measurements of nuclei A and B1 from the archival VLA data. We find that the flux densities of both nuclei were consistent with their historical values at epoch 2004.84, whereas the 8.4-GHz flux density of B1 had approximately doubled in 2006.29.

Our best estimate for the change in the flux density of B1 is an increase of approximately 6.5 mJy between 2004.84 and 2006.29. Given the estimated supernova rate of only $\sim 0.11 \text{ yr}^{-1}$ in B1 (Alonso-Herrero et al. 2000), it seems reasonable to attribute this entire

increase to the single new source we have detected in our VLBI observations. Given that assumption, Figure 8 shows an 8.4 GHz light curve for the Arp 299 radio supernova, using the combination of archival VLA data and VLBI observations. The supernova in Arp 299 reached a peak power of at least $1.2 \times 10^{21} \text{ W Hz}^{-1}$ at 8.4 GHz, about 2,000 times the Cas A power. This is comparable to the peak radio powers of the luminous Type II_n supernovae summarized by Weiler et al. (2002). It is far more powerful than the late-time powers of Type Ibc supernovae (Soderberg et al. 2006), and nearly 10 times more powerful than the recently discovered radio supernova in M82 (Brunthaler et al. 2009).

We note the estimated supernova rates of 0.65 yr^{-1} for nucleus A and 0.11 yr^{-1} for B1 (Alonso-Herrero et al. 2000). Our 8.4-GHz VLBI observations and those of Neff et al. (2004) spanned a total of $\sim 2.5 \text{ yr}$; detection of one new supernova in each of A and B1 is consistent with those values, assuming that most of the young supernovae actually are detectable radio supernovae.

4.6. Supernovae as Signposts for Super Star Clusters

The new supernova in B1 appeared within two milliarcseconds, or 0.4 pc (projected), of a steady 2.3 GHz source with a flux density of 0.25 mJy; this 2.3 GHz source did not vary when the new source appeared. The four steady 2.3 GHz sources all lie within a rectangle about 100 by 160 mas, with a total area of $1.6 \times 10^4 \text{ mas}^2$. One can test the hypothesis that a new supernova occurring with equal probability at any location in this rectangle would appear very close to an existing source by chance. For a completely random location of the new supernova, the *a priori* probability that it would occur within 5 mas of an existing source is 2.0%, and the probability of occurrence within 2 mas of an existing source is 0.3%. Thus the likelihood is that the new supernova is physically associated in some way with the existing radio source. If the two radio sources actually are SNe/SNRs separated by 0.4 pc, their supernova shells would overlap in no more than 100 yr even for expansion speeds of only $2,000 \text{ km s}^{-1}$.

The most logical physical association is that both the older SNR and the new supernova are located in the same super star cluster (SSC) in nucleus B1. Such SSCs have typical radii of 4 pc in the Antennae (Whitmore et al. 1999), corresponding to 20 mas at Arp 299. In fact, the SSCs found nearby, such as R136 in 30 Doradus (Hunter et al. 1995), are highly centrally condensed, so massive stars and supernovae may be most likely to coexist over a much smaller region. Since the compact VLBI sources detected in B1 are otherwise separated by typical distances of 10–15 pc, it is tempting to hypothesize that each is a beacon identifying the location of an individual SSC. We note that a number of SSCs dominated

by thermal emission previously have been detected and imaged by the VLA (Turner et al. 2000; Beck et al. 2002; Johnson & Kobulnicky 2003; Turner & Beck 2004). However, the SSCs dominated by thermal emission apparently are younger than 3 Myr, whereas the possible SSCs indicated by our VLBI observations must be older than 3 Myr in order to harbor SNe and SNRs.

Statistical inferences based on single objects are, of course, quite perilous. However, Neff et al. (2004) also noted that the new 8.4-GHz source in nucleus A appeared within 3 pc (projected) of a previously detected 2.3-GHz source, and suggested that they might be in the same SSC. There are at least four compact radio sources in nucleus A within a projected separation of ~ 10 pc, making it likely that these are associated in some way. A deeper VLBI integration would reveal whether there are weaker SNRs physically associated with the same regions.

The possible confusion of radio sources at different frequency bands provides some cause for anxiety in considering the spectral indices of the eight objects apparently detected at both radio frequencies (see Section 4.3), because there is no guarantee that detections at multiple frequencies actually correspond to the same source. The eight multi-frequency objects do not vary significantly at 8.4 GHz over the course of 1.5 yr. Most appear to have optically thin synchrotron spectra, and thus are likely to be older SNRs radiating at both 2.3 and 8.4 GHz rather than chance coincidences. However, object 33.630+46.79 has a flat spectrum between 2.3 and 8.4 GHz, so it is possible that it is an SNR with an unusual spectrum or that it does, in fact, correspond to two confused sources.

4.7. Possible Active Galactic Nuclei

In recent years, there have been several reports that one or both of Arp 299 nuclei A and B (or B1) may be active galactic nuclei (AGNs). Della Ceca et al. (2002) detected a hard X-ray component in Arp 299; arcsecond-scale imaging by Zezas et al. (2003) indicated that nucleus B1 has a hard X-ray spectrum and may be an AGN, while spectral fits to nucleus A indicated that it too could have an AGN component. Tarchi et al. (2007) also found H₂O maser emission in both A and B1, supporting the possibility of dual AGNs in Arp 299.

Since we detect numerous radio sources in each nucleus, it is not possible to determine which (if any) might correspond to the X-ray sources. However, we can at least check whether the radio/X-ray ratios for our typical compact radio sources might be consistent with the presence of AGNs. We make use of the definition $R_X = \nu L_\nu(5 \text{ GHz})/L_X(2 - 10 \text{ keV})$ (Terashima & Wilson 2003). In nucleus B1, the X-ray source has an X-ray luminosity of

$\sim 7 \times 10^{39}$ ergs s^{-1} in the 0.1–10 keV range (Zezas et al. 2003); our typical compact radio source (excluding the single young supernova) has a strength of $\sim 200 \mu\text{Jy}$ at 5 GHz (based on the 2.3 GHz detections and spectral limits), giving $\nu L_\nu \sim 1 \times 10^{36}$ ergs s^{-1} , and $\log R_X \sim -3.8$ (ignoring relatively small corrections for the X-ray spectrum). The X-ray source in nucleus A emits $\sim 1 \times 10^{40}$ ergs s^{-1} (Zezas et al. 2003); the relatively strong 1 mJy radio source which Neff et al. (2004) speculated to be a possible AGN has $\nu L_\nu \sim 3 \times 10^{36}$ ergs s^{-1} at 5 GHz, so $\log R_X \sim -3.5$ if this radio source were associated with the X-ray emission, or somewhat lower (similar to Nucleus B1) if one of the weaker radio sources were the X-ray source. Thus our estimated values of $\log R_X \sim -4.0$ to -3.5 are consistent with the values of low-luminosity Seyfert galaxies observed by Terashima & Wilson (2003), and it is possible that one of the compact radio sources in either A or B1 (or both) may be an AGN. However, it also is possible that an AGN could have $\log R_X \sim -4.5$, and hence be undetected in the present VLBI observations. The best way to determine which of the compact radio sources might be an AGN may be to conduct a high-sensitivity phase-referenced VLBI observation of the H₂O masers in order to see if they could be identified with any of the compact continuum radio emitters.

Neff et al. (2004) hypothesized that VLBI resolution of source D could indicate whether it belongs to Arp 299 or is a background AGN. None of our four epochs of observations have resolved this radio source, so we suspect that the possible resolution on the scale of the beam size that was reported previously (Neff et al. 2004) may have been spurious. In fact, given the X-ray luminosity (Zezas et al. 2003) and average radio flux density of this object, it has $\log R_X \sim -2.3$, consistent with values found for some PG quasars by Terashima & Wilson (2003).

5. Summary

We have observed the nearby galaxy merger Arp 299 at four epochs and two frequencies with a long-baseline radio interferometer consisting of the VLBA and the GBT. The primary results of these observations are as follows:

1. Thirty compact radio sources were detected in the two primary merger nuclei above limits of 10–30 times the luminosity of Cas A. The 25 detections in nucleus A span a diameter of ~ 100 pc, while the 5 detections in nucleus B1 span a diameter of ~ 30 pc.
2. The ratios of the numbers of radio sources in nuclei A and B1 are consistent with the ratios of the supernova rates inferred by Alonso-Herrero et al. (2000).

3. Most sources have variability upper limits of $\sim 20\%$ over 18.5 months, consistent with the interpretation that they are relatively young supernova remnants.
4. A few objects were detected at 8.4 GHz and not at 2.3 GHz, indicating that they may be younger radio supernovae that are still optically thick at the lower frequency.
5. A previously detected young supernova in nucleus A had a steadily declining 8.4 GHz flux density over 2.5 yr, but still had not become detectable at 2.3 GHz after the same interval.
6. A new supernova was detected in nucleus B1, with an apparent explosion date in the first half of 2005; this object had a peak luminosity at least 2,000 times the Cas A power. The new supernova occurred within 2 mas (0.4 pc projected) of a previously known steady radio source; it is highly likely that these two radio sources are the signposts of a super star cluster that formed at least 3 Myr ago in nucleus B1.
7. Comparison of the radio powers of the individual sources to the X-ray luminosities of nuclei A and B1 indicates that it is possible that one radio source in each nucleus is actually an active galactic nucleus rather than a young SNR.

The National Radio Astronomy Observatory is a facility of the National Science Foundation operated under cooperative agreement by Associated Universities, Inc. I thank the many NRAO staff that made these observations possible. I also thank Susan Neff for assistance in early stages of this project, and for supplying figures from Neff et al. (2004). Finally, I thank the anonymous referee for suggestions that significantly improved the presentation of the paper.

Facilities: VLBA; GBT; VLA.

REFERENCES

- Aalto, S., Radford, S. J. E., Scoville, N. Z., & Sargent, A. I. 1997, *ApJ*, 475, L107
- Alonso-Herrero, A., Rieke, G. H., Rieke, M. J., & Scoville, N. Z. 2000, *ApJ*, 532, 845
- Baan, W. A., & Haschick, A. 1990, *ApJ*, 364, 65
- Baars, J. W. M., Genzel, R., Pauliny-Toth, I. I. K., & Witzel, A. 1977, *A&A*, 61, 99
- Ballo, L., Braitto, V., Della Ceca, R., Maraschi, L., Tavecchio, F., & Dadina, M. 2004, *ApJ*, 600, 634
- Beasley, A. J., & Conway, J. E. 1995 in *ASP Conf. Ser. 82, Very Long Baseline Interferometry and the VLBA*, eds. J. A. Zensus, P. J. Diamond, & P. J. Napier (San Francisco: ASP), 327
- Beck, S. C., Turner, J. L., Langland-Shula, L. E., Meier, D. S., Crosthwaite, L. P., & Gorjian, V. 2002, *AJ*, 124, 2516
- Brunthaler, A., Menten, K. M., Reid, M. J., Henkel, C., Bower, G. C., & Falcke, H. 2009, *A&A*, 499, L17
- Chevalier, R. A., & Fransson, C. 2001, *ApJ*, 558, L27
- Chevalier, R. A., Li, Z.-Y., & Fransson, C. 2004, *ApJ*, 606, 369
- Condon, J. J. 1992, *ARA&A*, 30, 575
- Cresci, G., Mannucci, F., Della Valle, M., & Maiolino, R. 2007, *A&A*, 462, 927
- Della Ceca, R., et al. 2002, *ApJ*, 581, L9
- Dickinson, M., Giavalisco, M., & The GOODS Team. 2003, in *The Mass of Galaxies at Low and High Redshift*, eds. R. Bender & A. Renzini (Springer-Verlag), 324
- Elmegreen, B. G. 2005, in *Starbursts: From 30 Doradus to Lyman Break Galaxies*, ed. R. de Grijs & R. M. González Delgado (Dordrecht: Springer), 57
- Fenech, D. M., Muxlow, T. W. B., Beswick, R. J., Pedlar, A., & Argo, M. K. 2008, *MNRAS*, 391, 1384
- Ferguson, H. C., Dickinson, M., & Williams, R. 2000, *ARA&A*, 38, 667
- Fey, A. L., et al. 2004, *AJ*, 127, 3587

- García-Marín, M., Colina, L., Arribas, S., Alonso-Herrero, A., & Mediavilla, E. 2006, *ApJ*, 650, 850
- Gehrz, R. D., Sramek, R. A., & Weedman, D. W. 1983, *ApJ*, 267, 551
- Giavalisco, M., et al. 2004, *ApJ*, 600, L93
- Greisen, E. W. 2003, in *Information Handling in Astronomy - Historical Vistas, Astrophysics and Space Science Library Vol. 285*, ed. A. Heck (Dordrecht: Kluwer), 109
- Henkel, C., Peck, A. B., Tarchi, A., Nagar, N. M., Braatz, J. A., Castangia, P., & Moscadelli, L. 2005, *A&A*, 436, 75
- Hughes, D. W. 1980, *Nature*, 285, 132
- Hunter, D. A., Shaya, E. J., Holtzman, J. A., Light, R. M., O’Neil, E. J., & Lynds, R. 1995, *ApJ*, 448, 179
- Johnson, K. E., & Kobulnicky, H. A. 2003, *ApJ*, 597, 923
- Kotilainen, J. K., Moorwood, A. F. M., Ward, M. J., & Forbes, D. A. 1996, *A&A*, 305, 107
- Kronberg, P. P., Sramek, R. A., Birk, G. T., Dufton, Q. W., Clarke, T. E., & Allen, M. L. 2000, *ApJ*, 535, 706
- Lai, O., Rouan, D., Rigaut, F., Doyon, R., & Lacombe, F. 1999, *A&A*, 351, 834
- Lenc, E., & Tingay, S. J. 2006, *AJ*, 132, 1333
- Lípari, S., Díaz, R., Taniguchi, Y., Terlevich, R., Dottori, H., & Carranza, G. 2000, *AJ*, 120, 645
- Lonsdale, C. J., Diamond, P. J., Thrall, H., Smith, H. E., & Lonsdale, C. J. 2006, *ApJ*, 647, 185
- Mattila, S., Monard, L. A. G., & Li, W. 2005, *IAU Circ.* 8473
- Meurer, G. R., Heckman, T. M., Leitherer, C., Kinney, A., Robert, C., & Garnett, D. R. 1995, *AJ*, 110, 2665
- Modjaz, M., Kirshner, R., Challis, P., & Berlind, P. 2005, *IAU Circ.* 8475
- Muxlow, T. W. B., Pedlar, A., Wilkinson, P. N., Axon, D. J., Sanders, E. M., & de Bruyn, A. G. 1994, *MNRAS*, 266, 455

- Napier, P. J., Bagri, D. S., Clark, B. G., Rogers, A. E. E., Romney, J. D., Thompson, A. R., & Walker, R. C. 1993, *Proc IEEE*, 82, 658
- Neff, S. G., & Ulvestad, J. S. 2000, *AJ*, 120, 670
- Neff, S. G., Ulvestad, J. S., & Teng, S. H. 2004, *ApJ*, 611, 186
- Norris, R. P., & Forbes, D. A. 1995, *ApJ*, 446, 594
- Parra, R., Conway, J. E., Diamond, P. J., Thrall, H., Lonsdale, C. J., Lonsdale, C. J., & Smith, H. E. 2007, *ApJ*, 659, 314
- Reed, J. E., Hester, J. J., Fabian, A. C., & Winkler, P. F. 1995, *ApJ*, 440, 706
- Rovilos, E., Diamond, P. J., Lonsdale, C. J., Lonsdale, C. J., & Smith, H. E. 2003, *MNRAS*, 342, 373
- Scoville, N., et al. 2007, *ApJS*, 172, 38
- Soderberg, A. M., Nakar, E., Berger, E., & Kulkarni, S. R. 2006, *ApJ*, 638, 930
- Soifer, B. T., Neugebauer, G., Matthews, K., Becklin, E. E., Ressler, M., Werner, M. W., Weinberger, A. J., & Egami, E. 1999, *ApJ*, 513, 207
- Tarchi, A., Castangia, P., Henkel, C., & Menten, K. M. 2007, *New Astronomy Reviews*, 51, 67
- Terashima, Y., & Wilson, A. S. 2003, *ApJ*, 583, 145
- Turner, J. L., & Beck, S. C. 2004, *ApJ*, 602, L85
- Turner, J. L., Beck, S. C., & Ho, P. T. P. 2000, *ApJ*, 532, L109
- Ulvestad, J. S., & Antonucci, R. R. J. 1994, *ApJ*, 424, L29
- Ulvestad, J. S., & Antonucci, R. R. J. 1997, *ApJ*, 488, 621
- Weiler, K. W., Panagia, N., Montes, M. J., & Sramek, R. A. 2002, *ARA&A*, 40, 387
- Whitmore, B. C., Zhang, Q., Leitherer, C., Fall, S. M., Schweizer, F., & Miller, B. W. 1999, *AJ*, 118, 1551
- Zezas, A., Ward, M. J., & Murray, S. S. 2003, *ApJ*, 594, L31

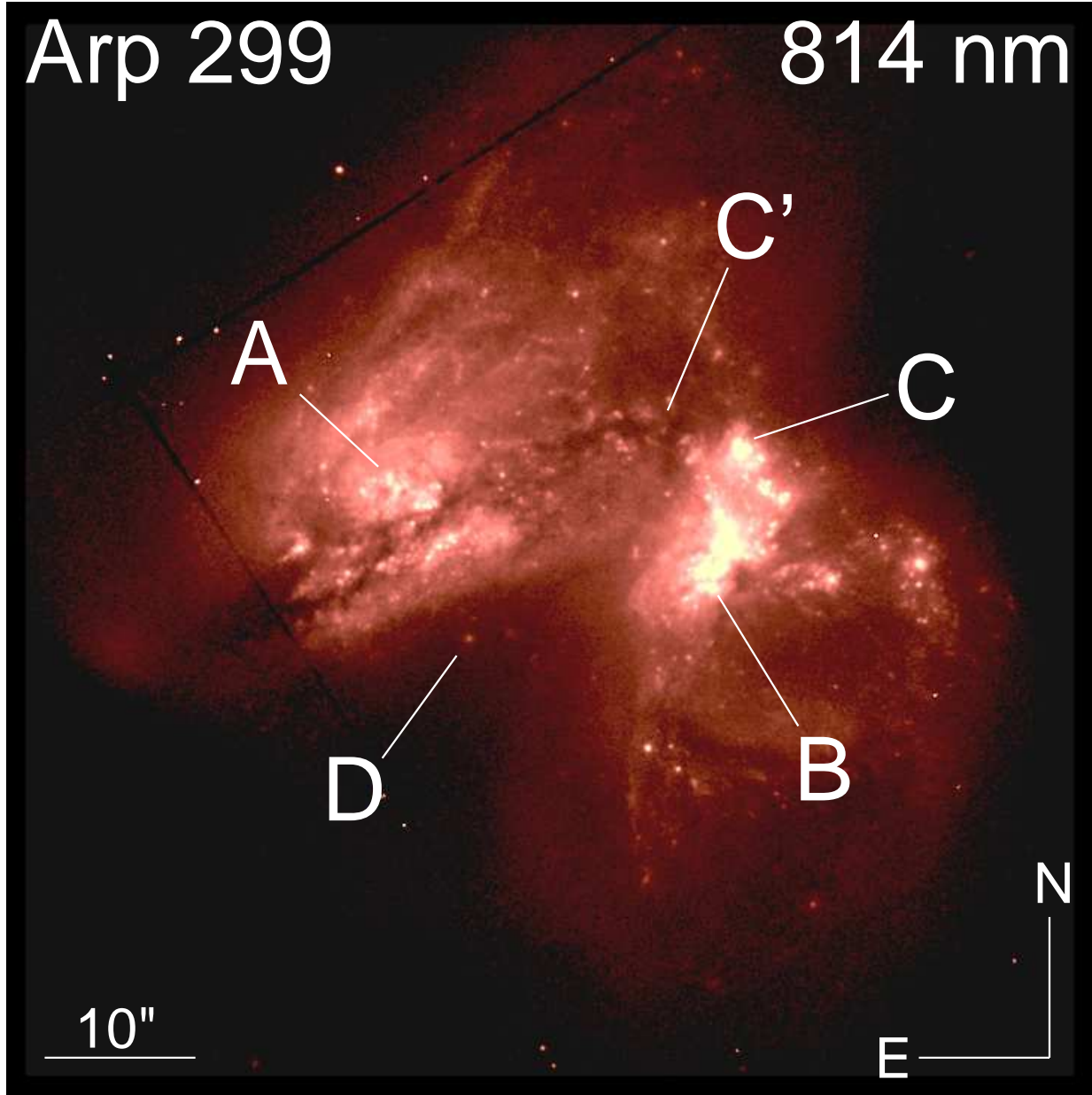


Fig. 1.— HST WFPC2 814 nm image of Arp 299, taken from Neff et al. (2004). The primary merger nuclei A and B, the possible smaller nuclei C and C', and the additional radio source D are all labelled. Reproduced by permission of the AAS.

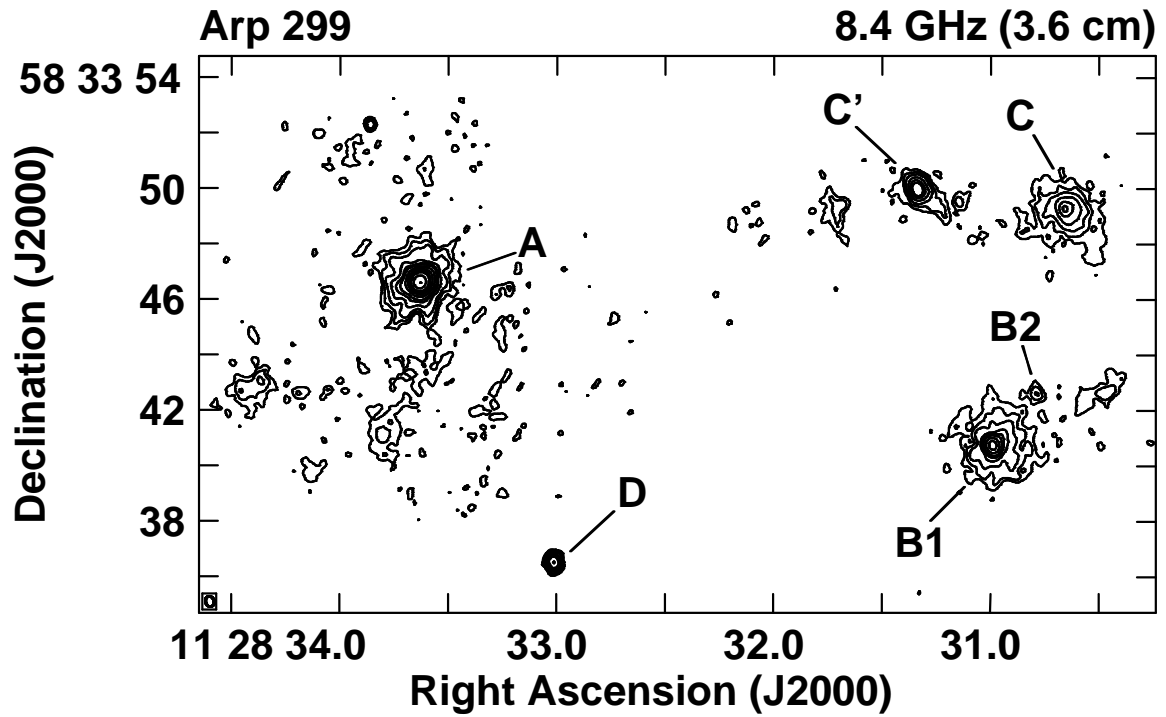


Fig. 2.— VLA 8.4 GHz image of Arp 299, taken from Neff et al. (2004). Labels are similar to those in Figure 1, except that nucleus B is separated into sources B1 and B2. Reproduced by permission of the AAS.

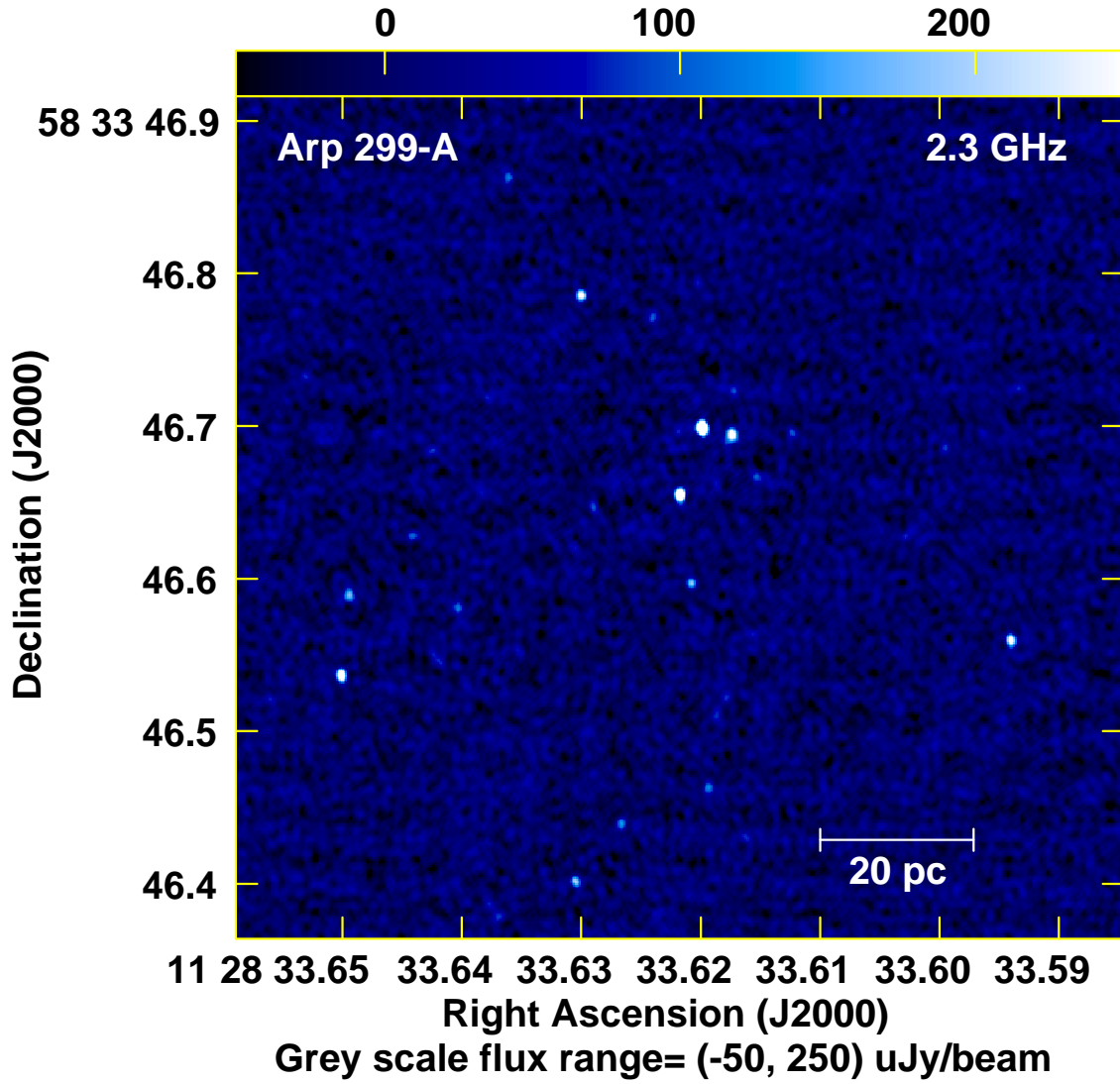


Fig. 3.— VLBI image of nucleus A of Arp 299 at 2.3 GHz, combining data from all four epochs. The intensity scale is shown at the top.

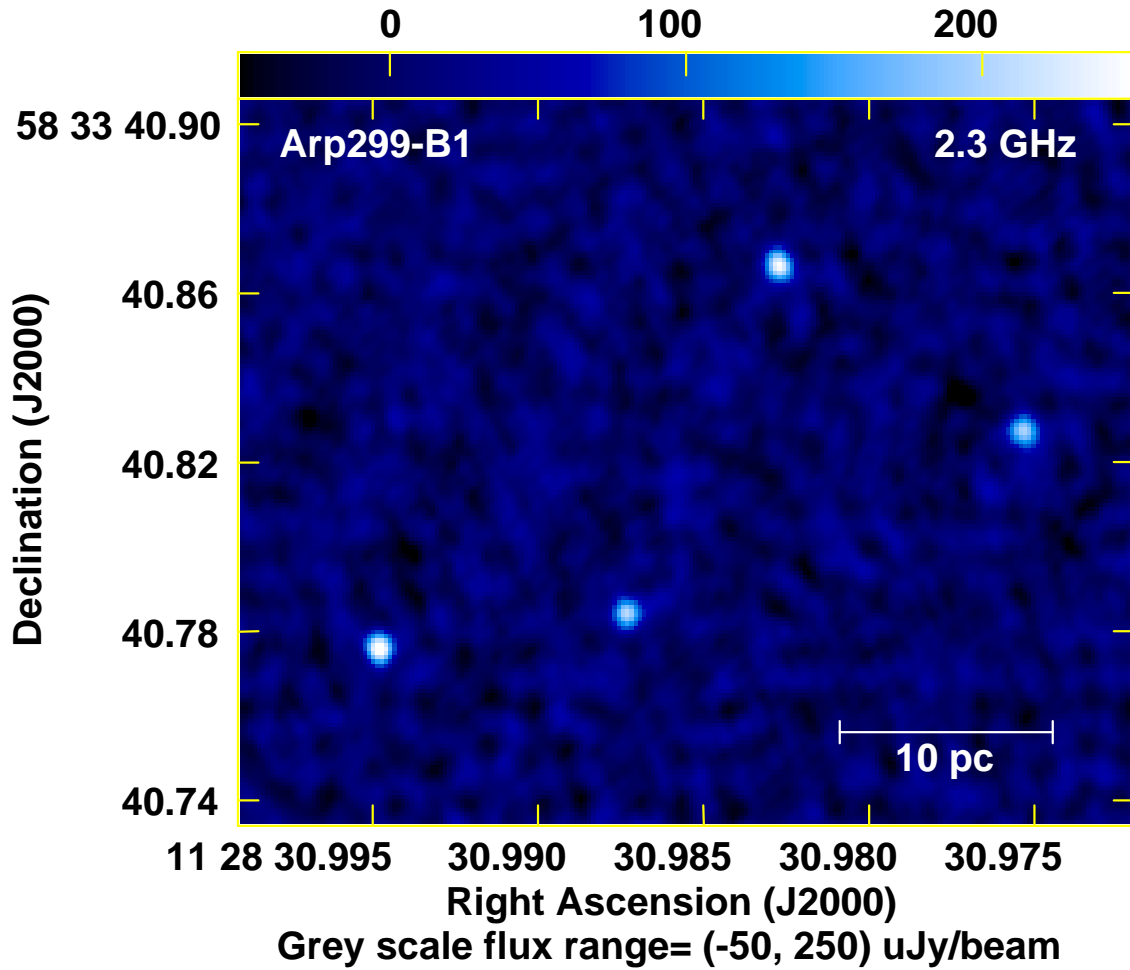


Fig. 4.— VLBI image of nucleus B1 of Arp 299 at 2.3 GHz, combining data from all four epochs. The intensity scale is shown at the top.

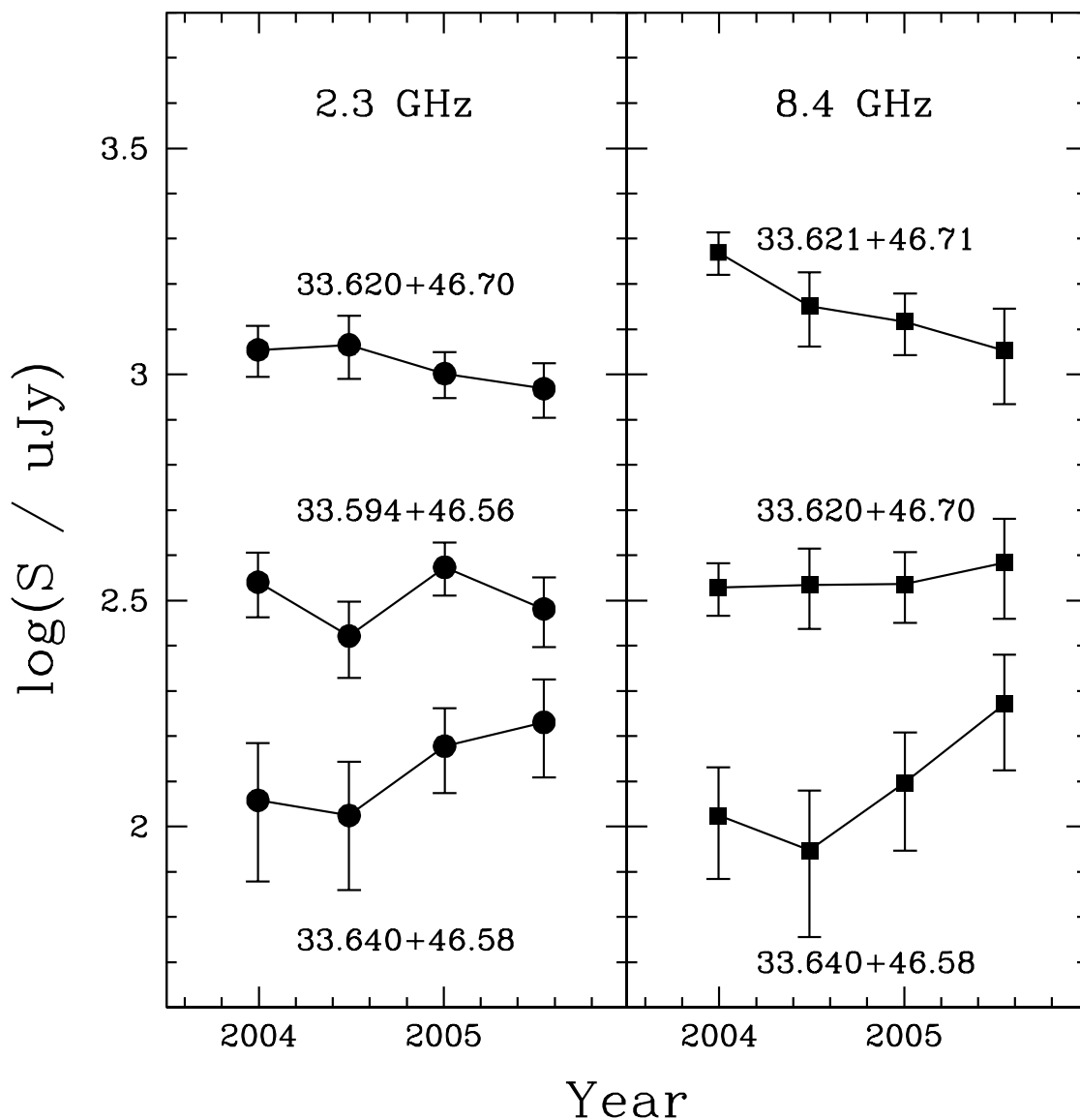


Fig. 5.— Time histories of strengths of compact sources at three different flux-density levels, in nucleus A, at 2.3 GHz (left) and 8.4 GHz (right). Each flux-density curve is labelled by the source designation. Two sources (33.620+46.70 and 33.640+46.58) are shown in both panels. The fading 8.4 GHz source, 33.621+46.71, is the apparent supernova reported previously by Neff et al. (2004).

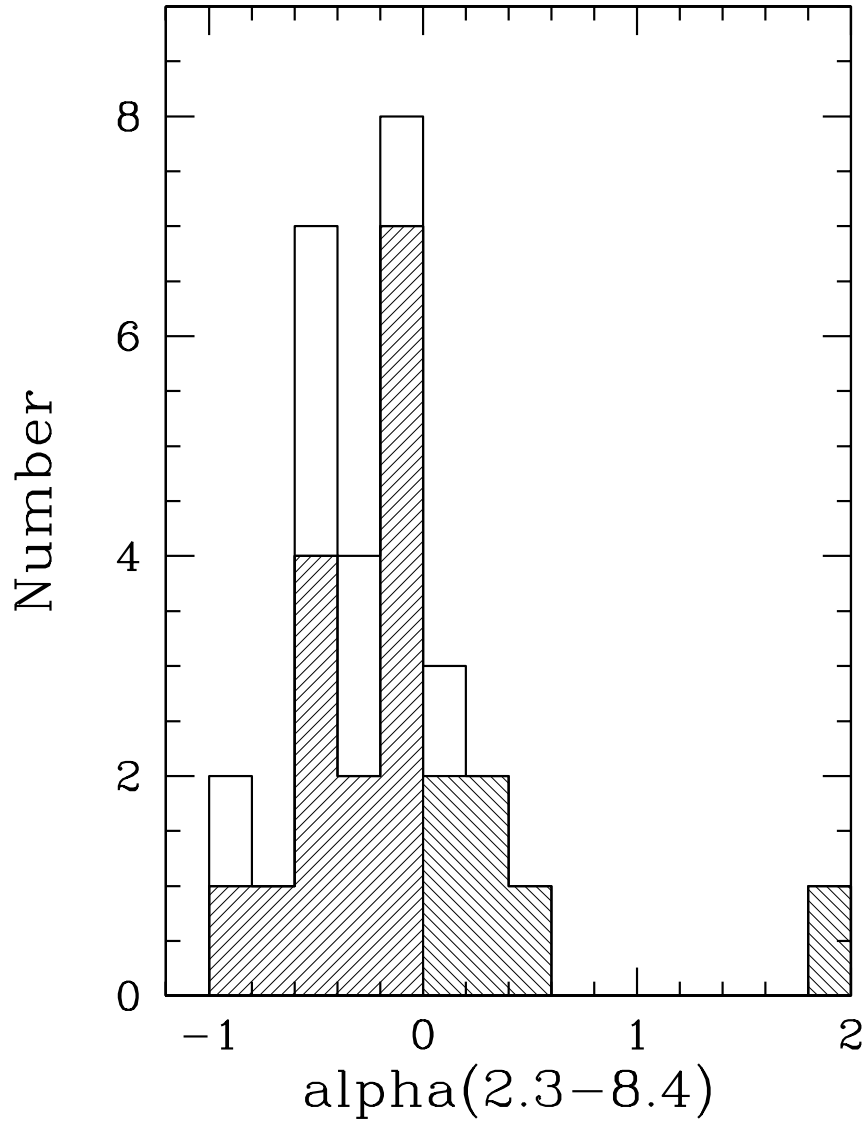


Fig. 6.— Distribution of two-point spectral indices of compact radio sources in nucleus A. Hatched values represent either lower limits ($\alpha > 0$) or upper limits ($\alpha < 0$), while the eight sources detected at both frequency bands are shown un-hatched.

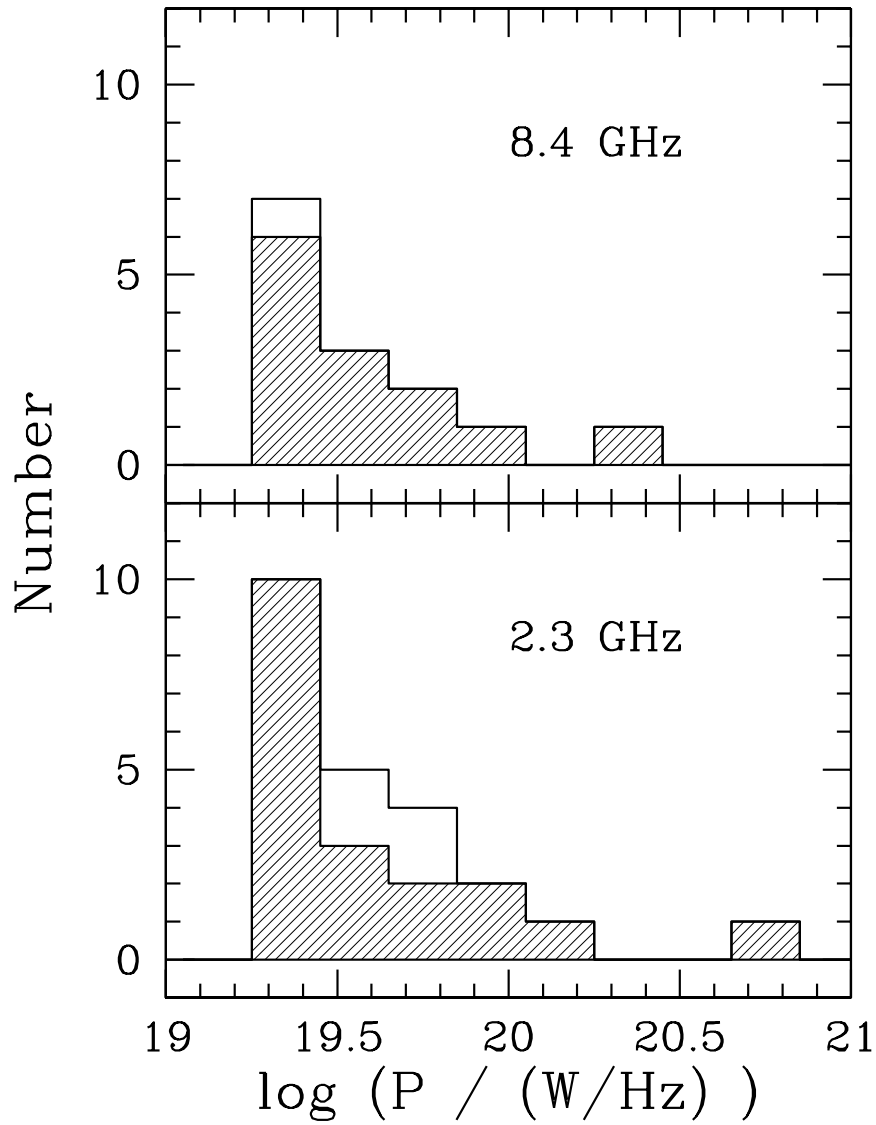


Fig. 7.— Histogram of radio luminosities of the compact radio sources in the two nuclei of Arp 299. The sources in nucleus A are shaded, while those in nucleus B1 are unshaded. The recent supernova in nucleus B1 is not included.

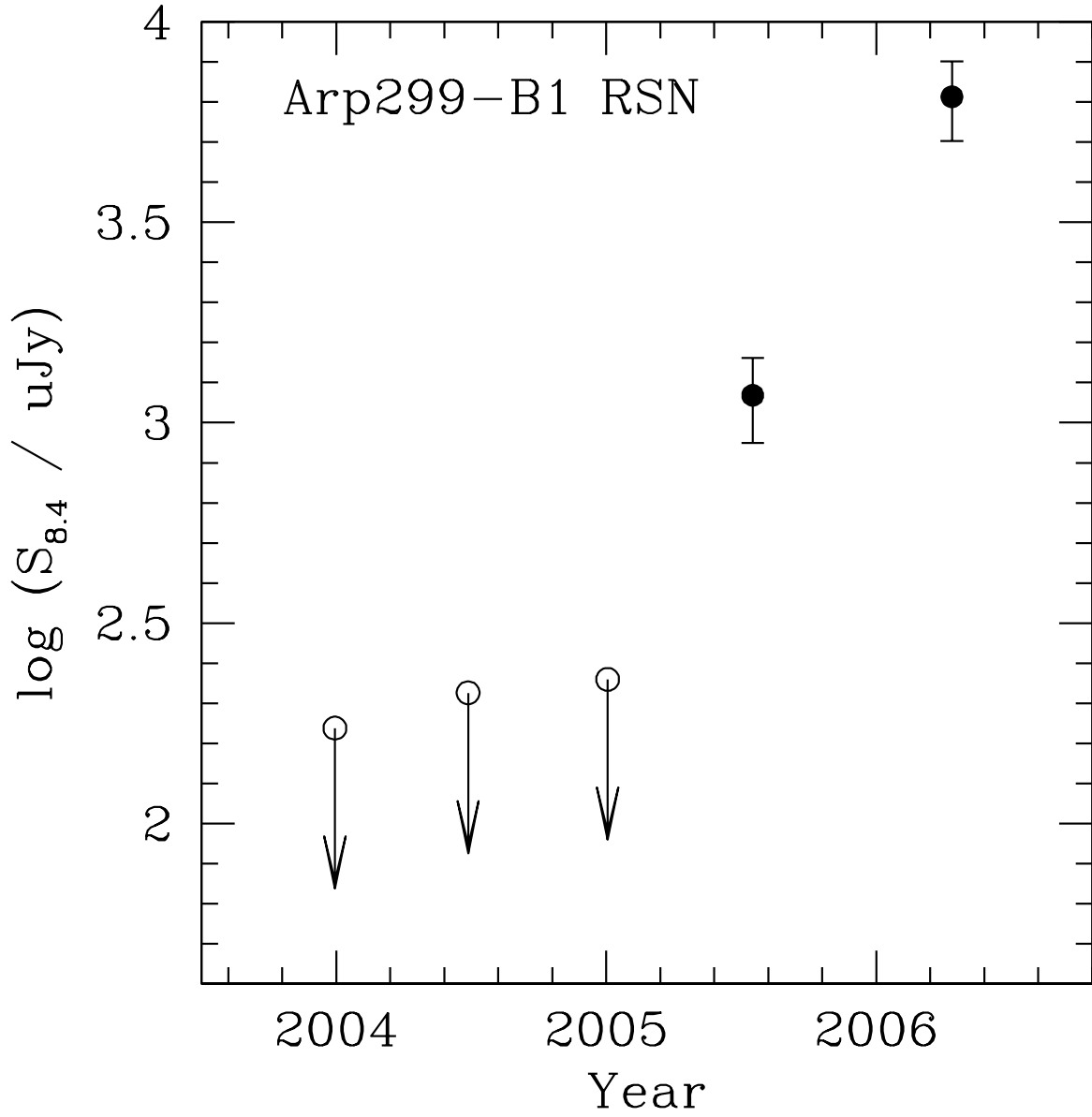


Fig. 8.— Light curve of radio supernova 30.988+40.78 in nucleus B1 at 8.4 GHz, showing four VLBI observations and the VLA archival observation from 2006.29. Open circles are 6σ upper limits from our VLBI observations, and 1σ error bars are shown on the two detections.

Table 1. VLBA+GBT Observations of Arp 299

(1) Date	(2) Sky Frequency (GHz)	(3) Integration (min)	(4) Resolution (milliarcsec)	(5) rms noise ^a ($\mu\text{Jy beam}^{-1}$)
2003 Dec 29	2.2715	178	6.80×5.37	36
	8.4215	180	1.93×1.31	27
2004 Jun 27	2.2715	178	6.29×4.69	29
	8.4215	181	1.76×1.14	27
2005 Jan 02	2.2715	172	6.37×4.97	27
	8.4215	173	2.16×1.19	31
2005 Jul 17	2.2715	174	6.49×4.85	35
	8.4215	176	1.84×1.16	30

^aThe “raw” rms noise for each individual image is given in this table. These values should be scaled upward by the amplitude correction factors shown in Table 2 to estimate the “true” noise values.

Table 2. Amplitude Correction Factors Caused by Coherence Losses

(1) Frequency	(2) 2003 Dec 29	(3) 2004 Jun 27	(4) 2005 Jan 02	(5) 2005 Jul 17	(6) Average	(7) Measured rms ($\mu\text{Jy beam}^{-1}$)	(8) Effective rms ($\mu\text{Jy beam}^{-1}$)
2.3 GHz	1.15	1.24	1.11	1.19	1.17	18	21
8.4 GHz	1.07	1.31	1.23	1.43	1.26	15	19

Table 3. Compact Sources Detected at 2.3 GHz

Name	α (J2000) 11 ^h 28 ^m	δ (J2000) 58°33'	Flux Density (μ Jy)	Comments
<u>Nucleus A</u>				
33.594+46.56	33.5941 ^s	46''560	354±32	Also at 8.4 GHz
33.612+46.70	33.6124 ^s	46''696	119±22	
33.615+46.67	33.6154 ^s	46''667	125±23	
33.617+46.72	33.6173 ^s	46''724	115±22	
33.618+46.70	33.6175 ^s	46''695	382±33	
33.619+46.46	33.6194 ^s	46''463	149±23	
33.620+46.70	33.6200 ^s	46''699	1090±76	Also at 8.4 GHz
33.621+46.60	33.6209 ^s	46''597	217±26	
33.622+46.66	33.6218 ^s	46''655	662±49	Also at 8.4 GHz
33.624+46.77	33.6241 ^s	46''771	121±23	
33.627+46.44	33.6267 ^s	46''440	165±24	
33.629+46.65	33.6290 ^s	46''647	114±22	
33.630+46.79	33.6301 ^s	46''786	335±31	Also at 8.4 GHz
33.631+46.40	33.6305 ^s	46''402	241±27	
33.636+46.86	33.6361 ^s	46''863	139±23	
33.640+46.58	33.6404 ^s	46''581	141±23	Also at 8.4 GHz
33.644+46.63	33.6442 ^s	46''628	126±23	
33.650+46.59	33.6495 ^s	46''589	211±25	Also at 8.4 GHz
33.650+46.54	33.6501 ^s	46''537	487±39	Also at 8.4 GHz
<u>Nucleus B1</u>				
30.975+40.83	30.9753 ^s	40''828	237±26	
30.983+40.87	30.9827 ^s	40''867	294±29	
30.987+40.78	30.9873 ^s	40''784	245±27	Near 8.4 GHz supernova
30.995+40.78	30.9948 ^s	40''776	332±31	Also at 8.4 GHz
<u>Source D</u>				
33.011+36.55	33.0109 ^s	36''549	964±68	Background?

Table 4. Compact Sources Detected at 8.4 GHz

Name	α (J2000) 11 ^h 28 ^m	δ (J2000) 58°33'	Flux Density (μ Jy)	Comments
<u>Nucleus A</u>				
33.594+46.56	33.5941 ^s	46''560	194±26	Also at 2.3 GHz
33.599+46.64	33.5992 ^s	46''637	132±22	
33.620+46.70	33.6199 ^s	46''699	371±38	Also at 2.3 GHz
33.621+46.71	33.6212 ^s	46''707	1410±126	Declining flux ^a
33.622+46.66	33.6218 ^s	46''655	504±49	Also at 2.3 GHz
33.628+46.62	33.6280 ^s	46''623	147±23	
33.630+46.79	33.6301 ^s	46''786	366±38	Also at 2.3 GHz
33.631+46.62	33.6307 ^s	46''620	214±27	
33.636+46.68	33.6356 ^s	46''677	141±23	
33.639+46.55	33.6391 ^s	46''550	129±22	
33.640+46.58	33.6402 ^s	46''580	118±22	Also at 2.3 GHz
33.650+46.59	33.6495 ^s	46''591	159±24	Also at 2.3 GHz
33.650+46.54	33.6501 ^s	46''537	267±30	Also at 2.3 GHz
<u>Nucleus B1</u>				
30.988+40.78	30.9875 ^s	40''784	1170±280	Fourth epoch only
30.995+40.78	30.9948 ^s	40''776	153±23	Also at 2.3 GHz
<u>Source D</u>				
33.011+36.55	33.0108 ^s	36''549	1810±161	Background?

^aThe flux densities of source 33.621+46.71 at the four new observing epochs were as follows. 2003 Dec 29: $1861 \pm 199 \mu$ Jy; 2004 Jun 27: $1416 \pm 264 \mu$ Jy; 2005 Jan 02: $1308 \pm 204 \mu$ Jy; 2005 Jul 17: $1128 \pm 269 \mu$ Jy. These also are plotted in the upper right portion of Fig. 5.

Table 5. VLA 8.4-GHz Flux Densities of Arp 299

Epoch	$S_{8.4}$ (mJy)	
	Nucleus A	Nucleus B1
2004.84	72.7 ± 3.6	7.1 ± 0.4
2006.29	64.4 ± 6.4	13.6 ± 1.4